FERROELECTRICS

Ferroelectricity in untwisted heterobilayers of transition metal dichalcogenides

Lukas Rogée[1]†, Lvjin Wang[2]†, Yi Zhang[1], Songhua Cai[1], Peng Wang[3], Manish Chhowalla[4]*, Wei Ji[2]*, Shu Ping Lau[1]*

Two-dimensional materials with out-of-plane (OOP) ferroelectric and piezoelectric properties are highly desirable for the realization of ultrathin ferro- and piezoelectronic devices. We demonstrate unexpected OOP ferroelectricity and piezoelectricity in untwisted, commensurate, and epitaxial MoS_2/WS_2 heterobilayers synthesized by scalable one-step chemical vapor deposition. We show d_{33} piezoelectric constants of 1.95 to 2.09 picometers per volt that are larger than the natural OOP piezoelectric constant of monolayer In_2Se_3 by a factor of ~6. We demonstrate the modulation of tunneling current by about three orders of magnitude in ferroelectric tunnel junction devices by changing the polarization state of MoS_2/WS_2 heterobilayers. Our results are consistent with density functional theory, which shows that both symmetry breaking and interlayer sliding give rise to the unexpected properties without the need for invoking twist angles or moiré domains.

The rational vertical integration of two-dimensional (2D) materials has led to exciting condensed matter effects that have opened different avenues of research. These interesting effects are a consequence of the interactions between the layers of atomically thin materials that give rise to moiré superlattices, hybrid electronic structures, and breaking of the usual crystal symmetries (*1*). Materials such as graphene and bilayer 2H MoS_2 are centrosymmetric (*2*). In contrast, odd numbers of layers of 2D materials such as MoS_2 are noncentrosymmetric, belonging to the $\bar{6}m2$ point group (or D_{3h}), and therefore exhibit in-plane (IP) piezoelectricity. Noncentrosymmetric 2D materials also generate second harmonic emission that can be used to confirm the absence of inversion symmetry. The magnitude of the IP piezoelectric component, referred to as d_{11} (or d_{22} if the armchair direction of the lattice is indexed as 2), has been estimated to be ~2.5 to 4 pm V^{-1} for single-layer MoS_2 (*3*). Materials of the $\bar{6}m2$ point group do not exhibit out-of-plane (OOP) piezoelectricity (*4*).

OOP piezoelectricity in 2D materials has been reported in few-layered In_2Se_3 (*5*) and by introducing chalcogen vacancies in $MoTe_2$ (*6*). Theoretical studies have explored the piezoelectric properties of transition metal dichalcogenide (TMDC) alloys when assembled into vertical heterostructures (*7*). Recently, ferroelectricity has been observed in twisted layers of hexagonal boron nitride (h-BN) and TMDCs (*8*, *9*). The origin of ferro- and piezoelectricity in twisted bilayers arises from the formation of moiré lattices and interlayer sliding (*10*). Ferro- and piezoelectricity have also been observed in rhombohedral homobilayer TMDCs (*11*). However, OOP piezoelectric and ferroelectric effects in epitaxially grown, untwisted, commensurately stacked, laterally large vertical heterostructures of 2D TMDCs have not been experimentally reported.

We have developed a simple one-step chemical vapor deposition (CVD) process to grow commensurate MoS_2/WS_2 heterobilayers on SiO_2 substrates that possess measurable OOP ferroelectricity and an OOP piezoelectric component d_{33}, even though individual layers of WS_2 and MoS_2 have $d_{33} = 0$. We explain this observation by taking the heterobilayer to be one crystal system with its own point group. In the case of the CVD-grown MoS_2/WS_2 heterobilayers we studied, the point group is $3m$ (or C_{3v}), which lacks the vertical symmetry to nullify OOP strain effects and thus possesses a nonzero d_{33} component that has a magnitude of up to 2.09 pm V^{-1}. A special subgroup of piezoelectrics are also ferroelectric; that is, their internal electric polarization can be switched between two stable states via an external electric field. Ordinary 2D TMDCs are not known to exhibit any ferroelectric characteristics (*12*). The classification of MoS_2/WS_2 heterobilayers as $3m$ point group materials suggests that they could be ferroelectric. We confirm this via piezoresponse measurements at room temperature. We demonstrate ferroelectric tunnel junctions (FTJs) based on MoS_2/WS_2 heterobilayers, which use the switchability of the ferroelectric to control the tunneling current density through the device (*13*).

We show an example of our CVD-grown heterobilayers (Fig. 1), which shows smaller WS_2 triangles (lateral dimensions of ~10 μm) draped by a larger MoS_2 monolayer (lateral dimensions of up to 200 μm). The size and shape of the triangles can be changed through variations in the growth recipe [see texts S1 and S2 (*14*)]. We performed detailed Raman analysis from different regions on the sample (Fig. 1B), which shows pure single-layer MoS_2 (region labeled as α, IP vibrational mode E′ at ~383 cm^{-1} and OOP vibrational mode A'_1 at ~403 cm^{-1}). The triangles labeled with β show Raman signals from both MoS_2 and WS_2 (E′ mode of WS_2 at ~355 cm^{-1} and its A'_1 mode at ~417 cm^{-1} along with the MoS_2 peaks). We also show a scanning electron microscope (SEM) image of a large MoS_2 layer covering a smaller WS_2 triangle (Fig. 1C). We obtained cross-sectional high annular angle dark field scanning transmission electron microscope (HAADF-STEM) images from two regions (Fig. 1C, labeled d and e). MoS_2 and WS_2 can be easily distinguished in our cross-sectional STEM images by the higher contrast of the W atoms that make the WS_2 layer noticeably brighter than the MoS_2 layer. Bright-field STEM (BF-STEM) images provide additional evidence of the bilayer structure (see text S3). We performed chemical analysis of the heterobilayers using energy-dispersive x-ray spectroscopy (EDS) to confirm the chemical composition of the heterobilayers (see text S4). The larger MoS_2 layer draping over the edge of the WS_2 layer is clearly visible in the cross-sectional image (Fig. 1D). The interior region of the bilayer (Fig. 1E) clearly shows an MoS_2 layer on top of WS_2. We also collected additional photoluminescence (PL) and selected-area electron diffraction (SAED) data about the CVD-grown materials (see text S5).

We studied the stacking angle between MoS_2 and WS_2 by second harmonic generation (SHG) emission (Fig. 1G) (texts S6 and S7), which depends directly on the interlayer rotation angle θ (*15*). MoS_2 and WS_2 exhibit broad absorption at energies above 2.5 eV (*16*); thus, incident photons with a wavelength of 900 nm (1.37 eV) readily induce SHG emissions of 450 nm (2.74 eV) in both layers. In short, SHG emissions interfere entirely constructively (bright signal) when θ = 0° where the stacking sequence is similar to the 3R stacking in TMDC crystals (Fig. 1H). Conversely, when the stacking angle is θ = 60° (or 180°, 300° and so on because of three-fold rotation symmetry of TMDCs around the *c* axis) as in the 2H-phase TMDCs, the layers interfere entirely destructively and produce a dark signal.

Vertical bilayer heterostructures are often associated with the appearance of moiré patterns, which can have a substantial impact

[1]Department of Applied Physics, Hong Kong Polytechnic University, Hung Hom, Kowloon, Hong Kong, P. R. China. [2]Department of Physics and Beijing Key Laboratory of Optoelectronic Functional Materials and Micro-Nano Devices, Renmin University of China, Beijing 100872, P. R. China. [3]College of Engineering and Applied Sciences and Collaborative Innovation Center of Advanced Microstructures, Nanjing University, Nanjing 210093, P. R. China. [4]Department of Materials Science and Metallurgy, University of Cambridge, Cambridge, UK.
*Corresponding author. Email: apsplau@polyu.edu.hk (S.P.L.); wji@ruc.edu.cn (W.J.); mc209@cam.ac.uk (M.C.)
†These authors contributed equally to this work.

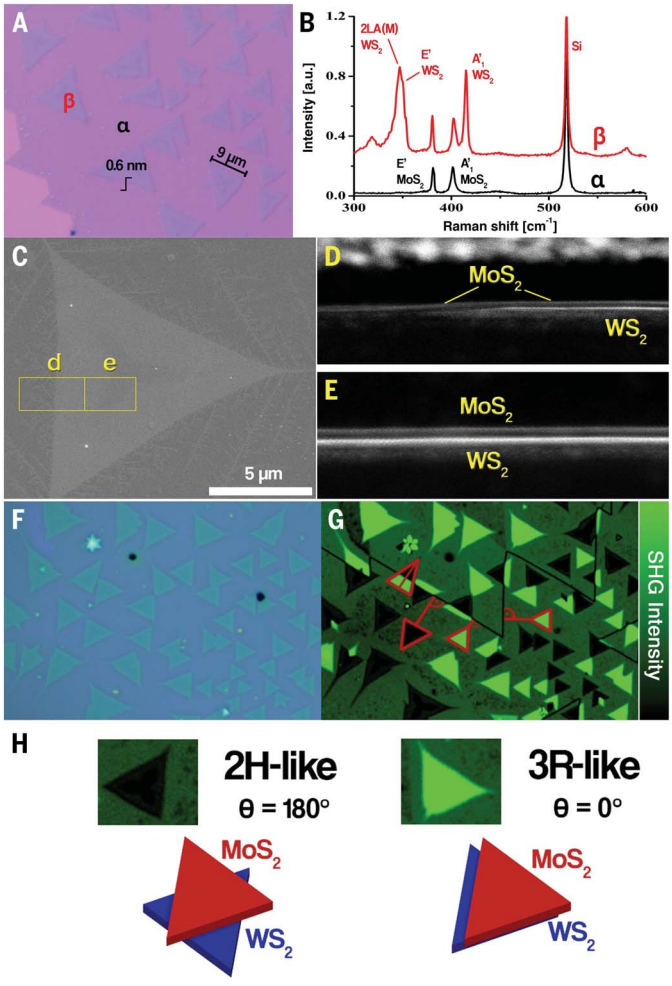

Fig. 1. CVD-grown MoS_2/WS_2 heterobilayers. (**A**) Optical microscope image of the as-grown heterobilayers showing smaller (~10 μm) WS_2 triangles draped over by a larger (~200 μm) MoS_2 layer. The thicknesses of the triangle edges were measured by AFM to be 0.6 nm—the thickness of a TMDC monolayer. (**B**) Raman spectra from α and β regions labeled in (A). The α regions show typical MoS_2 signals, whereas the β region shows both WS_2 and MoS_2 peaks. (**C**) Planar SEM image of a typical as-grown triangle. The two yellow rectangles *d* and *e* indicate regions selected for cross-sectional STEM imaging as shown in (D) and (E), respectively. (**D** and **E**) In region D, the MoS_2 layer draping over the brighter WS_2 layer is observed. In region E, a uniform bilayer consisting of MoS_2 on top of WS_2 can be seen. (**F**) Optical microscopy image of MoS_2/WS_2 triangles across a large MoS_2 cluster. (**G**) The corresponding unfiltered SHG intensity map. Note that there is no bare SiO_2 substrate visible in the image. The MoS_2/WS_2 triangles appear either very bright or very dark across the map. The black lines are single-crystal domain boundaries of the large MoS_2 monolayer. Bright triangles always point toward the nearest domain boundaries; dark triangles point away from them, as indicated by the red lines. (**H**) Relationship between SHG intensity and vertical stacking angle θ. Dark triangles are labeled 2H-like and bright triangles 3R-like.

on their piezo- and ferroelectric properties. In our case, the epitaxial heterobilayers do not show any moiré patterns (see text S8). Briefly, naturally grown bilayer TMDCs in either 2H or 3R stacking do not show moiré superlattices because their layers are commensurate. This property is not exclusive to homobilayers. MoS_2 and WS_2 have virtually identical lattice parameters (*16*, *17*) and as a consequence, heterobilayers of MoS_2 and WS_2 with a twist angle of $n \cdot 60°$ (with n being an integer) also do not show moiré superlattices. Our heterobilayers grown by CVD naturally align with each other in energetically ideal arrangements (i.e., epitaxially), consistent with epitaxially grown $WSe_2/MoSe_2$ heterobilayers (*18*) that also show an absence of moiré patterns because they also possess identical lattice constants. Commensurate stacking of different TMDC monolayers cannot yet be achieved by artificial stacking. A small difference in lattice constant between MoS_2 and WS_2 of 0.01 Å has been reported, but studies have shown that heterobilayers with lattice constant differences of up to 2% can become commensurate during the CVD growth. An example is CVD-grown monolayer graphene on Ni(111), which, despite a small lattice mismatch, reproduces a 1×1 commensurate heterolattice (*19*).

We show (fig. S9A) the edge of two heterobilayers with the same orientation. At this scale, outlines of moiré patterns would become apparent in artificially stacked bilayers with small stacking angles. However, this is not the case for our CVD samples. The corresponding fast Fourier transform (FFT) spectrum of the image shows a single hexagonal crystal pattern similar to the SAED pattern (fig. S6D). Moiré patterns are also absent in the STEM image of another sample (fig. S9B) of 3R-like and 2H-like heterobilayers. We collected the FFT spectra for the entire image, the individual 3R-like and 2H-like stacked heterobilayers as well as that of only MoS_2. All four FFT spectra are the same, which suggests no misalignment or twisting between the two layers. We therefore do not need to invoke twisting or moiré lattices to describe the origins of piezo- and ferroelectricity in our CVD-grown heterobilayers.

Piezoelectric mapping

Both 3R-like and 2H-like MoS_2/WS_2 heterobilayers can be treated as materials belonging to the $3m$ (or C_{3v}) point group that should exhibit a nonzero OOP piezoelectric constant d_{33} and potentially be ferroelectric. We have therefore investigated both properties using piezoresponse force microscopy (PFM) (DART-SS-PFM mode, Asylum Research) (*14*, *20*). In short, we created an alternating electric field (at voltage V_{AC}) locally using a conductive atomic force microscope (AFM) tip, which causes piezoelectric materials to deform and the magnitude of the deformation is measured and mapped. For PFM measurements, we transferred heterobilayers onto conductive substrates to avoid electrical charging during the measurements. We show SHG maps of triangles with different vertical stacking arrangements (Fig. 2A) and their corresponding AFM images (Fig. 2B). The two different stacking arrangements of MoS_2/WS_2 heterobilayers appear very similar in the AFM. We performed resonance-amplified PFM to obtain the OOP piezoelectric constant, mapping the results at different voltages between 1.2 and 2.0 V (Fig. 2C). We set the color scale of the PFM maps such that the mean height change of the pure MoS_2 is zero, and its color is green. This helps to account for possible electrostrictive effects from the background because MoS_2 by itself does not exhibit OOP piezoelectricity. The results show that with increasing voltage, the color contrast between the MoS_2/WS_2 heterobilayer and the pure MoS_2 monolayer significantly increases (Fig. 2C). That is, notable OOP piezoelectricity is indicated by the red color in the PFM maps.

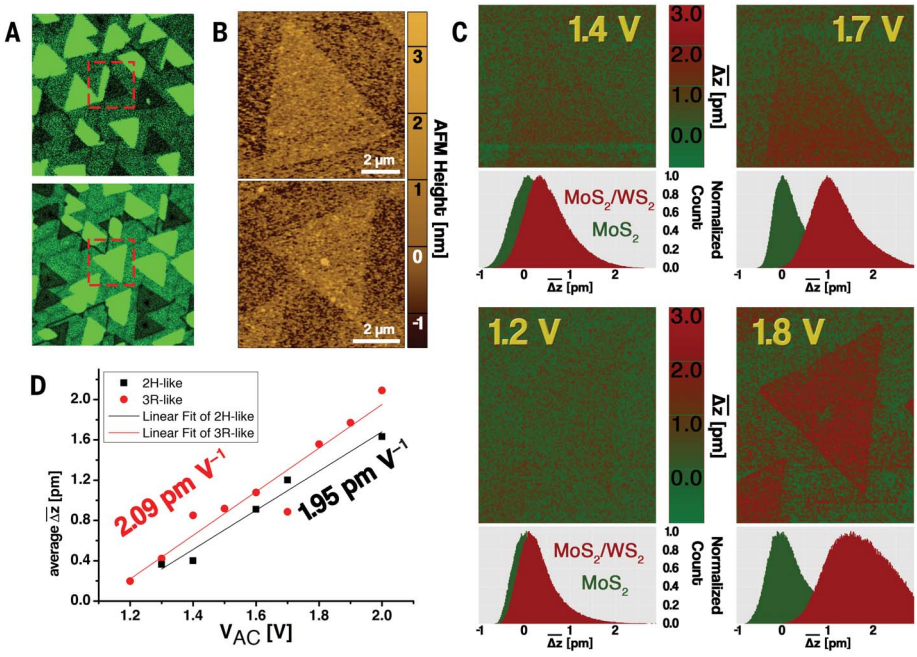

Fig. 2. PFM data of MoS_2/WS_2 heterobilayers on a conductive Pt-coated substrate. (**A**) SHG maps showing the triangles that were chosen for the PFM measurements. The upper triangle is largely 2H-like. The lower triangle is 3R-like. (**B**) AFM maps of the 2H-like and 3R-like triangles. The materials are atomically smooth with RMS roughness of ~0.1 nm. (**C**) Real piezoelectric height change $\overline{\Delta z}$ maps of both triangles, measured at different drive voltages V_{AC}. The distributions below each map show the piezoelectric height change for the MoS_2/WS_2 triangles (red) and the surrounding monolayer MoS_2 (green). (**D**) Plot of the average values of $\overline{\Delta z}$ as a function of V_{AC}.

Table 1. Overview of several 2D materials and their measured piezoelectric constants.

Material	Piezoelectric constant	Experimental value (pm V^{-1})
2H-like MoS_2/WS_2	d_{33}	1.95
3R-like MoS_2/WS_2	d_{33}	2.09
Monolayer MoS_2 (*35*)	d_{11}	3.78
Monolayer WSe_2 (*36*)	d_{11}	5.2
Monolayer α-In_2Se_3 (*5*)	d_{33}	0.34

The average of the vertical piezoelectric deformation $\overline{\Delta z}$ of multiple 2H-like and 3R-like triangles was obtained by rigorous statistical analysis (see text S9) to find the piezoelectric height change on the vertical heterostructures relative to the background. We plotted the $\overline{\Delta z}$ distributions for both the background and heterobilayers below each PFM map to show that the distance between the background and triangle distributions increases with increasing voltage, as we expected for OOP piezoelectricity. The distribution for the triangles also gets broader. This trend is because the real value of d_{33} varies slightly across the area of a triangle, and these slight differences multiplied by an increasing voltage V_{AC} result in ever greater contrast between the extremes of $\overline{\Delta z}$. We have plotted the average of $\overline{\Delta z}$ as a function of V_{AC} for both stacking types along with their respective linear fits (Fig. 2D).

The OOP piezoelectric component can be calculated using $d_{33} = \partial(\overline{\Delta z})/\partial V_{AC}$. We find $d_{33} = 1.95 \pm 0.2$ pm V^{-1} and 2.09 ± 0.2 pm V^{-1} for 2H-like and 3R-like stacked MoS_2/WS_2, respectively. We compare this to other experimentally obtained piezoelectric constants of other 2D materials (Table 1). We find that our measured data are similar in magnitude to the IP d_{11} piezoelectric constant of monolayer MoS_2 and substantially larger than the OOP d_{33} constant of monolayer α-In_2Se_3 (*5*). We also see that the stacking orientation of the heterostructure has a slight influence on its piezoelectric constant. As a result of the difference in stacking, the relative positions of W, Mo, and S atoms are different, which ultimately influences the magnitude and direction of the internal polarization. Spurious OOP piezoelectric effects can arise when the root mean square (RMS) roughness is higher than the thickness of TMDCs (>1.5 nm) (*21*). The AFM images (Fig. 2B) show that this is not the case in our samples because the heterobilayers are atomically smooth with RMS surface roughness of ~0.1 nm. This value is considerably less than the thickness of the heterobilayer, hence the OOP deformation we reported is intrinsic.

Ferroelectric hysteresis

The observation of a piezoelectric response in MoS_2/WS_2 heterobilayers does not necessarily imply the presence of ferroelectricity; however, the *3m* point group classification indicates that it is possible (*12*, *22*). Room-temperature ferroelectricity in stacked large-area CVD-grown TMDCs could open up possibilities for exciting electronics applications. We thus investigated the ferroelectric response of the heterobilayers (Fig. 3). First, we applied the DART-SS-PFM hysteresis method to our sample (*14*). The OFF-field phase loop (Fig. 3A) shows the typical shape obtained from domain switching in ferroelectric materials. The polarization switching occurs at the coercive voltage of ~V_{DC} = ±3 V in the heterobilayers. The corresponding OFF-field $\overline{\Delta z}$ loop exhibits the typical ferroelectric butterfly shape. Generally, the OFF-field piezoresponse hysteresis loops are used to investigate the ferroelectric performance to avoid spurious electrostrictive and electrochemical forces that can otherwise also cause piezoresponse loops that appear similar to ferroelectric ones (*23*). The butterfly loop is slightly offset toward the negative voltage direction. This behavior is indicative of small influences from nonferroelectric artifacts, such as charge injection, which is a common feature in ultrathin ferroelectrics (*24*). A phase loop is also apparent in the corresponding ON-field hysteresis loops (Fig. 3B), although it is more abrupt. The ON-field $\overline{\Delta z}$ loop appears as a large V-shape with a small butterfly pattern. These two shapes show that the ferroelectric and electrostrictive deformation coexist as long as a strong unidirectional electric field is present. Some nonferroelectric materials such as Al_2O_3 exhibit piezoresponse hysteresis loops even in OFF-field loops, which can be mistaken to be of ferroelectric origin (*25*, *26*). We show through variation of the drive voltage V_{AC} that the ferroelectricity we observed is intrinsic (see text S10). We provide further evidence of ferroelectricity through domain writing (*14*). We poled a large area of the heterobilayer (with –8 V tip bias) and

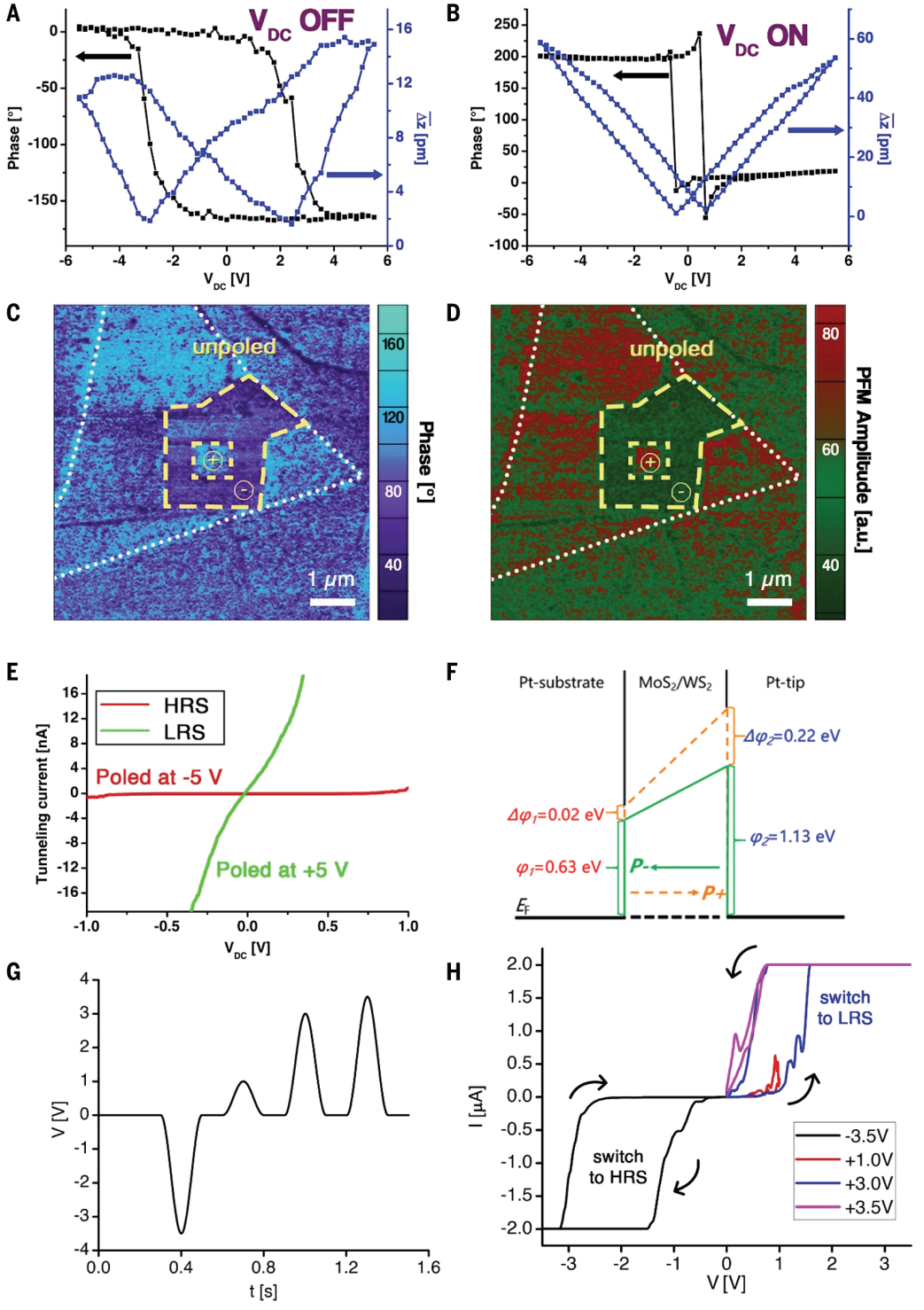

Fig. 3. Ferroelectricity in MoS_2/WS_2 heterobilayers. Piezoelectric hysteresis loops were measured by applying DC voltage sweeps from −5.5 to +5.5 V at 2.7 V AC drive voltage using DART-SS-PFM. (**A**) Phase and $\overline{\Delta z}$ hysteresis loops with the DC field OFF. (**B**) Phase and $\overline{\Delta z}$ hysteresis loops with the DC field ON. (**C** and **D**) Two square-shaped domains were written onto a heterobilayer triangle with −8 V for the outer square and 8 V for the inner square. The entire triangle is outlined by a dotted white line for clarity. The phase map (C) and PFM amplitude map (D) show that the poled areas, marked by dashed yellow outlines, do not extend beyond the boundaries. (**E**) Polarization-dependent tunneling current versus applied DC field through an FTJ device. The tunneling current is strongly dependent on the previous poling voltage. The ratio between the low- and high-resistance states (LRS and HRS) is 10^2 to 10^3. (**F**) Schematic of the tunneling potential barrier change for the LRS and HRS states for an FTJ. Electron tunneling is reduced when the device is poled with a negative voltage, and increased with a positive poling voltage. (**G**) Switching voltage program applied to an FTJ for more in-depth analysis. A negative poling voltage pulse of −3.5 V is applied, followed by three positive voltage pulses with increasing magnitudes of 1 V, 3 V, and 3.5 V. (**H**) The corresponding *I-V* loop. The arrows indicate the direction of the current change.

a smaller square within that area (+8 V tip bias). These shapes are outlined in the phase and amplitude maps performed after poling (Fig. 3, C and D). They show a strong change in both the phase direction as well as the PFM amplitude in the designated areas.

To translate the fundamental ferroelectric properties into a practical demonstration, we measured the properties of FTJ devices based on the heterobilayers. The V_{DC}-dependent tunneling current in a FTJ can be substantially modified by poling the device prior to measurements (Fig. 3E). The device characteristics are also similar to ferrodiode behavior as reported by Liu *et al.* (*27*). Thus, although we use the term FTJ to describe our device, distinguishing between the two requires additional observations. In this case, negative poling with –5 V diminishes the electron tunneling current and puts the device in a high-resistance state (HRS), whereas positive poling of +5 V puts it in a low-resistance state (LRS). The ratio of the tunneling resistance between the two states reaches a value of 10^2 to 10^3. We show schematically how modification of the tunnel barrier with polarization of the ferroelectric (*13*, *28*–*30*) increases or decreases the

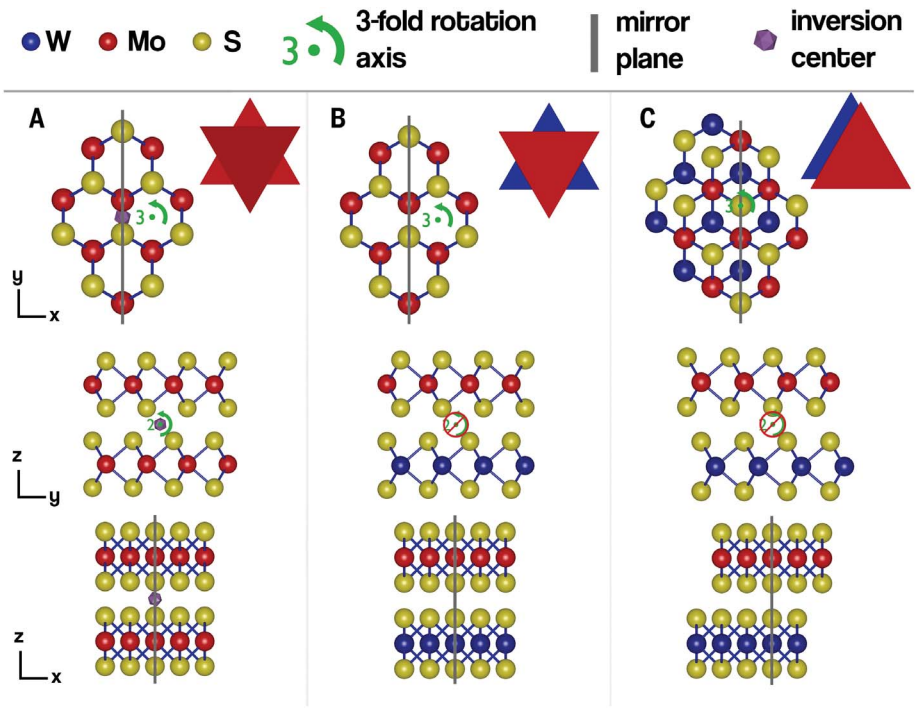

Fig. 4. Crystal symmetry models. (**A** to **C**) Schematic representation of bilayer 2H MoS_2 (A), 2H-like (B), and 3R-like heterostructure (C) of MoS_2/WS_2 from three different perspectives as indicated by the coordinate axes. The *c* direction (out-of-plane direction) is along the *z* axis, the zigzag direction is along the *x* axis, and the armchair direction is along the *y* axis.

tunneling current (Fig. 3F) (*31*, *32*). We have modeled our FTJ as a dual-slab made up of the MoS_2/WS_2 bilayer sandwiched by platinum slabs (see text S11). To reflect the real experimental setup, we increased the distance between the bilayer and the top electrode by 2 Å to model their weak interaction (fig. S11, E to H). Further, we have repeatedly applied a resistance-switching voltage program to an FTJ (Fig. 3G) to test for robustness. For each measurement cycle, we applied a strong negative voltage pulse (−3.5 V) to the sample to ensure that it is poled in the HRS. Then, we applied three positive voltage pulses of 1 V, 3 V, and 3.5 V. The resulting tunneling current measurements (Fig. 3H) show that the negative voltage induces HRS. The application of the 1-V pulse increases and decreases the current along the HRS curve without forming an open loop. Once the 3-V pulse is applied, an open loop is created where the sample switches from HRS to LRS, and the 3.5-V pulse simply follows the LRS curve without any open loop because resistance switching has already occurred. These measurements confirm that a voltage of at least the coercive voltage is needed to switch between the FTJ states, in accordance with the PFM data from Fig. 3A. More detailed poling experimental data on the same and other devices can be found in (*14*). Our overall hysteresis results indicate that MoS_2/WS_2 heterobilayers, as a *3m* point group material, exhibit ferroelectric properties at room temperature.

Crystal symmetries

TMDCs are known to show IP piezoelectric properties but no OOP piezoelectric properties (*4*, *33*). In accordance with the rules of group theory (see text S13), bilayer 2H MoS_2 belongs to the $\bar{3}^{2}_{m}$ (or D_{3d}) point group. We depict a schematic model of its crystal structure (Fig. 4A), which includes an inversion center. Ferroelectricity and piezoelectricity (also SHG) do not occur if an inversion center is present in a crystal. The 2H-like MoS_2/WS_2 heterobilayer (Fig. 4B) crystal structure is like bilayer 2H MoS_2 with the exception that Mo atoms are replaced with W atoms in the bottom layer. This makes a substantial difference to the crystal symmetry but does not lead to the appearance of moiré patterns because the lattice parameters of the two materials and their epitaxial growth are similar. As a result, all symmetry transformations that exchange atoms between the top and bottom layers become invalid, including the inversion center. The symmetry transformations that are left put the heterobilayer into the *3m* (or C_{3v}) point group. The same symmetry transformations also apply for 3R-like MoS_2/WS_2 (Fig. 4C) Hence, both stacking types belong to the same point group. The *3m* point group has exactly one nonzero OOP piezoelectric constant, d_{33}. *3m* point group materials also classify as polar materials because they have a unique rotation axis, no inversion center, and no mirror plane perpendicular to the rotation axis (*12*). This allows ferroelectricity to be possible from a geometric standpoint.

Theoretical derivation of strain-piezoelectric constant and mechanism of ferroelectric switching

We measured the strain-piezoelectric constant (d), which cannot be directly obtained from density functional theory (DFT) calculations. However, we can derive it from the stress-piezoelectric constant (e) and the elastic constant tensor (C) using the relation $d = eC^{-1}$, which can be obtained from DFT calculations. The OOP component of the strain piezoelectric constant tensor d_{33}, as measured in our PFM experiment, is theoretically derived from $d_{33} = [(C_{11} + C_{12})e_{33} - 2C_{13}e_{31}]/[(C_{11}+C_{12})C_{33} - 2C_{13}^2]$ (see text S14).

We determined the vertical strain piezoelectric constants of 2H-like and 3R-like MoS_2/WS_2 heterobilayers to be 2.28 pm V^{-1} and 2.40 pm V^{-1}, respectively. Both the absolute values of the two d_{33} constants, 2.28 and 2.40 pm V^{-1}, and their difference, 0.12 pm V^{-1}, are close to experimentally measured values (i.e., 1.95, 2.09, and 0.14 pm V^{-1}, respectively).

According to our calculations, both heterobilayers show spontaneous nonzero OOP electric polarizations, namely P_{out}[2H-like] = 0.44 pC m^{-1} and P_{out}[3R-like] = 0.60 pC m^{-1}. Switching their OOP polarization directions is not likely to be accessible by vertically moving any atoms, but could be achieved by a lateral sliding between the two monolayers in each of the heterobilayers, showing ferroelectric behavior. We show that the atomic structures of two stacking configurations (i.e., AA-up and AA-down) of the 3R-like heterobilayer differ from one another by a 1.83 Å lateral sliding along the armchair direction (see text S15). Configuration AA-up has an OOP polarization of 0.60 pC m^{-1} that is 1.9 meV/f.u. more stable than configuration AA-down with a negative value of −1.45 pC m^{-1}. An external electric field over 2.4 V/nm could switch their relative stability and thus, together with thermal excitation at finite temperatures, trigger the sliding occurrence surmounting a 16 meV/f.u. barrier, which accompanies reversal of polarization direction, displaying an explicit ferroelectric switching behavior.

The interfacial differential charge densities (DCD, a measure of charge variation at the interface) of two related AA-like (i.e., 3R-like for our particular case) stacking configurations of the heterobilayers explicitly show charge redistribution between the top and bottom layers that are illustrated as separation of the red (electron accumulation) and green (electron

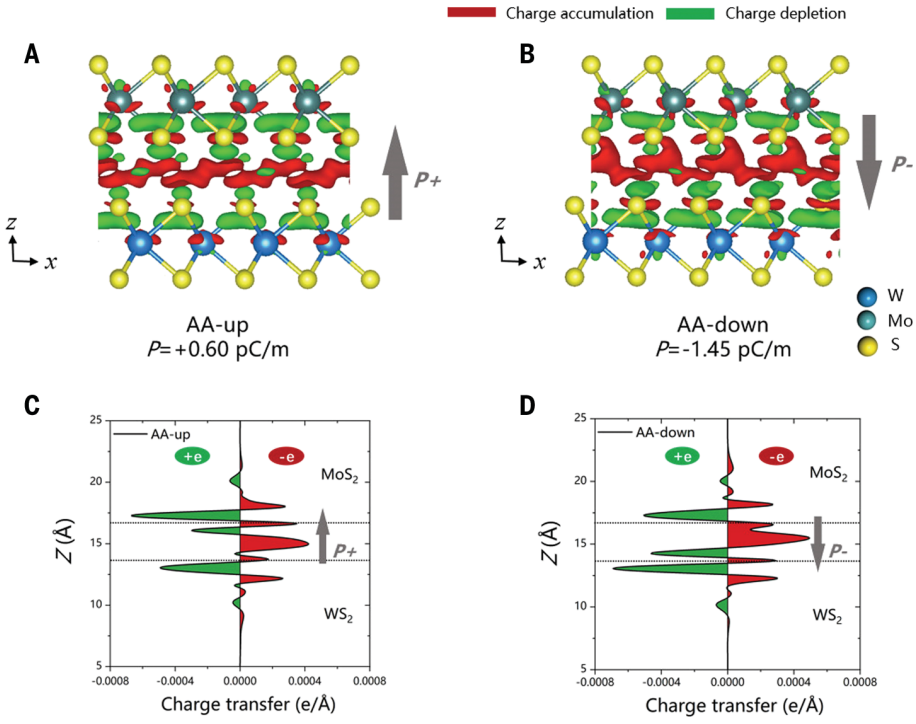

Fig. 5. Charge density plots. (**A** and **B**) Interlayer differential charge density for the up (AA-up) and down (AA-down) polarizations, respectively. An iso-surface value of 7×10^{-5} e/bohr^3 was used. (**C** and **D**) Their line profiles along *z*, respectively.

depletion) regions (Fig. 5). Their line profiles show explicit electric polarization at the interfaces and the direction of polarization is switchable under lateral sliding of one layer across roughly one-third of the unit cell. Our calculations give a switching barrier of 16 meV/f.u. This is comparable to the value of 9 meV/f.u. predicted by Li *et al.* (*34*) in BN bilayers where the authors used the sliding mechanism. This mechanism was also used to explain those experimentally observed ferroelectric effects by Stern *et al.* (*10*) and Yasuda *et al.* (*9*) in a temperature range from 4.2 K to 300 K.

Conclusion

This work demonstrates that ferro- and piezoelectricity can be found in untwisted commensurate bilayers consisting of monolayers of MoS_2 and WS_2. The heterobilayer is easy to grow in large quantities through a one-step CVD process, which does not require any precision transfer method or setup to realize, and can be scaled through variations in the growth recipe. Previous research on heterostructure ferroelectricity relied on the local moiré structures. In contrast, our material is free from any periodic superstructure and can be explained by a group theory approach for each entire bilayer type. This approach could be applied to other bottom-up heterostructures.

REFERENCES AND NOTES

1. A. Weston *et al.*, *Nat. Nanotechnol.* **15**, 592–597 (2020).
2. S. Islam, S. S. Z. Ashraf, *Resonance* **24**, 445–457 (2019).
3. C. Cui, F. Xue, W.-J. Hu, L.-J. Li, *npj 2D Mater. Appl.* **2**, 18 (2018).
4. A. H. Meitzler, IEEE Standard on Piezoelectricity. *ANSI/IEEE Std 176-1987*, 0_1 (1988).
5. F. Xue *et al.*, *ACS Nano* **12**, 4976–4983 (2018).
6. D. Seol *et al.*, *Nano Energy* **79**, 105451 (2021).
7. S. Yu, Q. Rice, B. Tabibi, Q. Li, F. J. Seo, *Nanoscale* **10**, 12472–12479 (2018).
8. A. Weston *et al.*, arXiv 2108.06489 (2021).
9. K. Yasuda, X. Wang, K. Watanabe, T. Taniguchi, P. Jarillo-Herrero, *Science* **372**, 1458–1462 (2021).
10. M. Vizner Stern *et al.*, *Science* **372**, 1462–1466 (2021).
11. X. Wang *et al.*, *Nat. Nanotechnol.* **17**, 367–371 (2022).
12. P.-P. Shi *et al.*, *Chem. Soc. Rev.* **45**, 3811–3827 (2016).
13. P. Hou *et al.*, *J. Mater. Chem. C* **6**, 5193–5198 (2018).
14. See supplementary materials.
15. W.-T. Hsu *et al.*, *ACS Nano* **8**, 2951–2958 (2014).
16. R. A. Bromley, R. B. Murray, A. D. Yoffe, *J. Phys. C* **5**, 759–778 (1972).
17. A. Molina-Sánchez, L. Wirtz, *Phys. Rev. B* **84**, 155413 (2011).
18. W.-T. Hsu *et al.*, *Nat. Commun.* **9**, 1356 (2018).
19. Y. Dedkov, E. Voloshina, M. Fonin, *Phys. Status Solidi B* **252**, 451–468 (2015).
20. Oxford Instruments, *Piezoresponse Force Microscopy with Asylum Research AFMs*; https://afm.oxinst.com/assets/uploads/products/asylum/documents/Piezoresponse-Force-Microscopy-AFM-web.pdf.
21. S. Kang *et al.*, *ACS Appl. Mater. Interfaces* **10**, 27424–27431 (2018).
22. D. Litvin, Ferroelectric Space Groups, *Acta Crystallogr. A* **42**, 44–47 (1986).
23. B. Kim, D. Seol, S. Lee, H. N. Lee, Y. Kim, *Appl. Phys. Lett.* **109**, 102901 (2016).
24. S. S. Cheema *et al.*, *Nature* **580**, 478–482 (2020).
25. Z. Guan *et al.*, *AIP Adv.* **7**, 095116 (2017).
26. H. Qiao, O. Kwon, Y. Kim, *Appl. Phys. Lett.* **116**, 172901 (2020).
27. X. Liu *et al.*, *Appl. Phys. Lett.* **118**, 202901 (2021).
28. R. Li *et al.*, *Appl. Phys. Lett.* **116**, 222904 (2020).
29. J. Wu *et al.*, *Nat. Electron.* **3**, 466–472 (2020).
30. S. Yuan *et al.*, *Nat. Commun.* **10**, 1775 (2019).
31. E. Y. Tsymbal, H. Kohlstedt, *Science* **313**, 181–183 (2006).
32. A. Gruverman, M. Alexe, D. Meier, *Nat. Commun.* **10**, 1661 (2019).
33. R. Hinchet, U. Khan, C. Falconi, S.-W. Kim, *Mater. Today* **21**, 611–630 (2018).
34. L. Li, M. Wu, *ACS Nano* **11**, 6382–6388 (2017).
35. S. K. Kim *et al.*, *Nano Energy* **22**, 483–489 (2016).
36. E. Nasr Esfahani, T. Li, B. Huang, X. Xu, J. Li, *Nano Energy* **52**, 117–122 (2018).

ACKNOWLEDGMENTS

Funding: Supported by Hong Kong Polytechnic University (grant 1-ZVGH), the Research Grants Council of Hong Kong (15306321, C5029-18E, AoE/P-701/20), the National Key R&D Program of China (grant 2018YFE0202700), the National Natural Science Foundation of China (grants 11622437, 11804247, 61674171, and 11974422), the Fundamental Research Funds for the Central Universities of China and the Research Funds of Renmin University of China (grant 22XNKJ30), and the Strategic Priority Research Program of Chinese Academy of Sciences (grant XDB30000000). This project has received funding from the European Research Council (ERC) under the European Union's Horizon 2020 research and innovation programme (grant agreement GA 101019828-2D-LOTTO)], Leverhulme Trust (RPG-2019-227), EPSRC (EP/T026200/1, EP/T001038/1), and Royal Society Wolfson Merit Award (WRM\FT\180009). **Author contributions:** S.P.L., M.C., and L.R. conceived this work. L.R., Y.Z., S.C., and M.C. performed materials characterization and analysis. L.W. and W.J. conducted theoretical calculations. HAADF-STEM imaging and analysis were performed by S.C. and P.W. M.C. wrote the manuscript with input from S.P.L., L.R., and W.J. All authors discussed the results and commented on the manuscript. **Competing interests:** The authors declare that they have no competing interests. **Data and materials availability:** All data are available in the manuscript or the supplementary materials.

SUPPLEMENTARY MATERIALS

science.org/doi/10.1126/science.abm5734
Materials and Methods
Supplementary Text
Figs. S1 to S13
References (*37*–*70*)

Submitted 28 September 2021; resubmitted 31 January 2022
Accepted 15 April 2022
10.1126/science.abm5734

Science

Ferroelectricity in untwisted heterobilayers of transition metal dichalcogenides

Lukas RogéeLvjin WangYi ZhangSonghua CaiPeng WangManish ChhowallaWei JiShu Ping Lau

Science, 376 (6596), • DOI: 10.1126/science.abm5734

Untwisted heterobilayers

Stacking two-dimensional materials can lead to a range of interesting and useful properties. For example, the emergence of piezo and ferroelectricity can occur by twisting the layers relative to each other. Rogée *et al*. used a different strategy for obtaining these sorts of properties by stacking alternating layers of molybdenum disulfide and tungsten disulfide, which breaks symmetry without requiring twisting. The authors show that these vapor-deposited heterobilayers can be made into a ferroelectric tunnel junction device. —BG